V1   Come svolgere una ricerca di fuga su una specifica flangia di un apparato appartenente ad un acceleratore lineare.

V2   Nell'ambito dell'Ultra Alto Vuoto, quali sono gli accorgimenti principali nel progettare e preparare una camera.

V3   Discutere le diverse tipologie di tenute su flange, con riferimento al tasso di perdita ed al livello di vuoto, oltre che agli aspetti funzionali.

V4   Spiegare cosa è una fuga virtuale e quali possono essere gli accorgimenti progettuali per limitarle o evitarle

V5   Discussione sulle diverse tipologie di pompe da vuoto, con riferimento ai vari livelli di vuoto per cui queste sono impiegate.

V6   Evidenziare quali sono gli aspetti più importanti da considerare nei processi di saldatura per la costruzione di una camera da vuoto.

C1   Principali caratteristiche dei liquidi criogenici.

C1   Principali caratteristiche dei liquidi criogenici.

C2   Discutere gli elementi principali relativi alla trasmissione del calore in criogenia

C3   Criogenia all'azoto e all'elio liquido: analogie e differenze.

C4   Discutere gli elementi principali da tenere in considerazione nella progettazione di sistema criogenico (es. un criostato o una linea criogenica).

C5   Problematiche di sicurezza in criogenia

C6   Componenti tipici di un apparato criogenico.

3.2 Silicon sensors

3.2.1 Design and specifications

The design requirements for a precision hermetic MIP timing detector in the CMS endcap region requires a uniform and efficient device capable of operating with sufficient radiation resistance to maintain performance throughout the lifetime of the HL-LHC. To meet these needs the ETL will be instrumented with Ultra-Fast Silicon Detectors (UFSDs), planar silicon devices based on the Low-Gain Avalanche Detector (LGAD) technology [26, 27]. UFSDs incorporate a low, controlled gain in the signal formation mechanism, see Figure 3.5. Charge multiplication happens when the charge carriers are in electric fields above $E \approx 300$ kV/cm, when the electrons (and to less extent the holes) acquire sufficient kinetic energy to generate additional e/h pairs. The field value can be obtained by implanting an appropriate doping density ($N_D \approx 10^{16}$/cm^3) that locally generates very high fields when depleted. The gain has an exponential dependence on the electric field $N(l) = N_o e^{\alpha(E)l}$, where $\alpha(E)$ is a strong function of the electric field and l is the path length inside the high-field region. The gain layer is realized through the addition of a p-type implant and, to avoid breakdown, its lateral spread is controlled by deep n-doped implants, called Junction Termination Extension (JTE) . Typical gain values are in the 10–30 range, which is modest compared to gains of thousands or more in APDs or SiPMs. Three vendors have successfully produced optimized UFSDs, which have been tested by CMS and are being considered for providing the ETL sensors: Centro Nacional de Microelectronica (CNM), Barcelona [26, 65, 66], Fondazione Bruno Kessler (FBK) [67, 68], and Hamamatsu Photonics (HPK) [69, 70].

Achieving good time performance at low gain requires pixels (also called pads) with a size less than a few mm^2, to limit the sensor capacitance, implying that a large number of pixels are required to cover the 7.9 m^2 of each ETL endcap. The design studied in the 2017 CMS MTD Technical Proposal (TP) used very large sensors, 5×10 cm^2, with 3×1 mm^2 pixels. Our R&D and design optimization studies have led to an updated design that now features smaller sensors, 21×42 mm^2 with square pixel pads of 1.3×1.3 mm^2. We have prepared a wafer layout for these sensor sizes, as shown in Fig. 3.6, and are pursuing updated quotes with vendors. The adoption of smaller sensors and pixels relative to the TP design has two important cost saving advantages: (i) the smaller sensor size allows for a more efficient use of the 6-inch silicon wafers and (ii) smaller sensors have a higher yield, while the cost of the high- and low-voltage distributions might increase slightly because of the increased granularity. An important advantage of the new sensor design is that the pixel capacitance is halved, improving the timing performance of the ASIC.
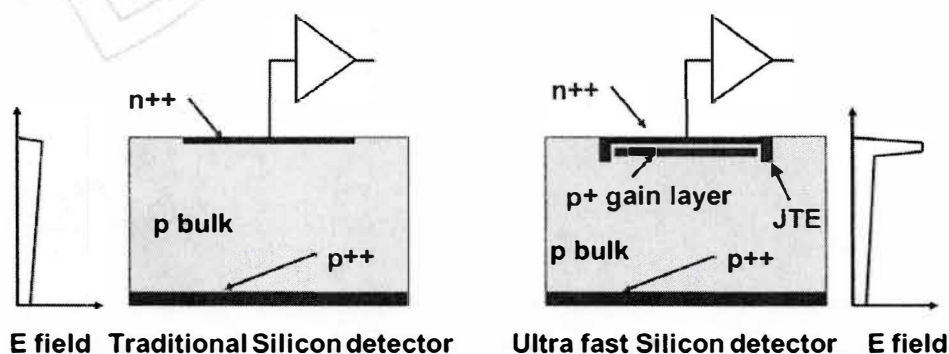

E field Traditional Silicon detector   Ultra fast Silicon detector   E field

Figure 3.5: Cross-sectional diagrams comparing a standard silicon detector and a UFSD with an additional p implant providing the larger electric field needed for charge multiplication.

807 # Chapter 2

808 # The Barrel Timing Layer

809 ## 2.1 Overview and principle of operation

810 The Barrel Timing Layer is designed as a cylindrical detector with a surface of about 38 m^2
811 capable of detecting MIPs with time resolution of 30 ps at the beginning of HL-LHC operation
812 and a luminosity-weighted resolution of about 45 ps. It is located between the ECAL and the
813 Tracker with an inner radius of 1148 mm and and outer radius of 1188 mm, as shown in Fig. 2.1.
814 It provides a coverage up to $|\eta| = 1.48$ with a geometric acceptance of about 90%, limited by
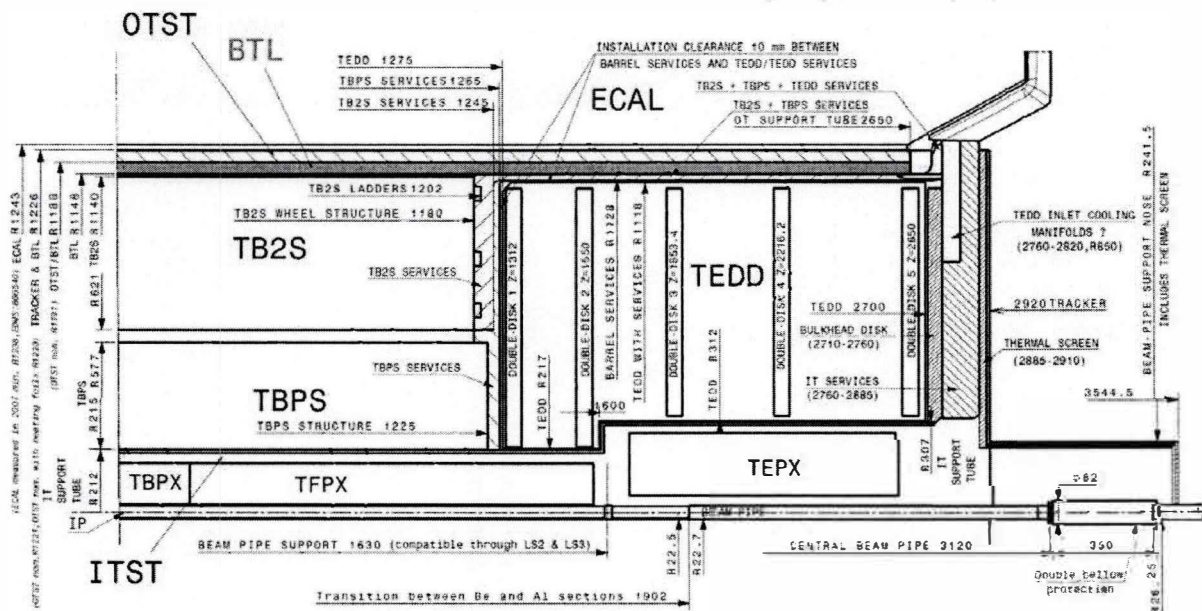815 the supporting rails of the Tracker and small dead areas between sensor modules.

Figure 2.1: BTL integration within CMS.

816 The sensitive elements consist of L(Y)SO:Ce crystal bars of about 57 mm length, 3.12 mm width
817 and an average thickness of ~3 mm read out by a pair of SiPMs, one at each end, matching the
818 size of the crystal end face for optimal light collection. The choice of this crystal geometry min-
819 imizes the SiPM area with respect to the crystal sensitive volume, limiting power consumption
820 and channel count, without loss of light collection efficiency, enabled by the total internal reflec-
821 tion occurring within crystals of such high aspect ratio. This sensor layout exploiting double-
822 ended readout also provides uniform time response across the surface, tracking capabilities
823 and redundancy of time measurements per crystal. The area of a single crystal represents the
824 optimal trade off between channel count and sensor performance. In particular, the chosen
825 granularity provides an average occupancy of the detector cells at pileup 200 of about 7%, thus
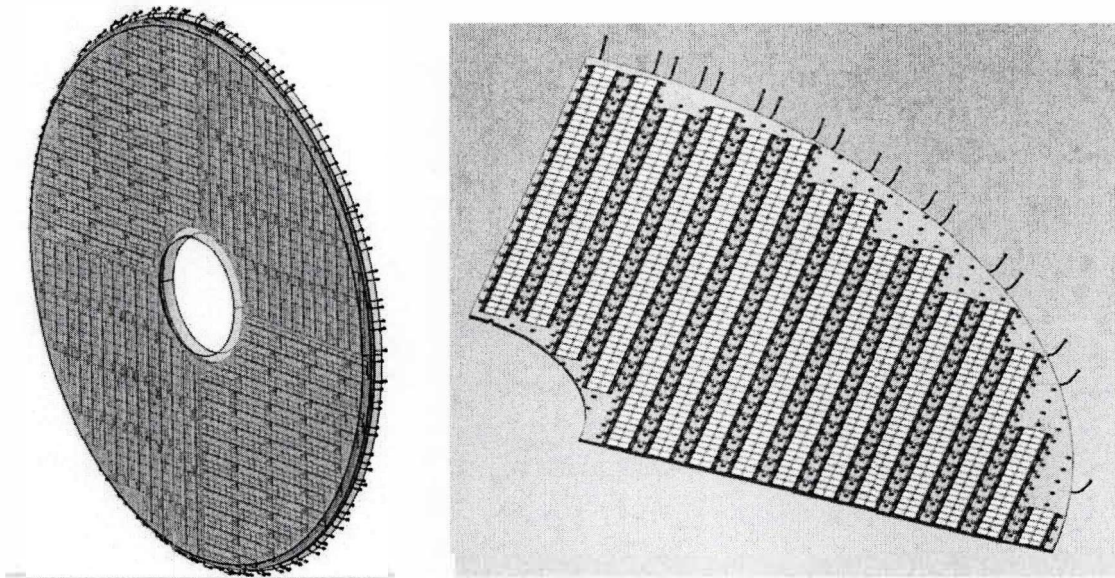
21

Figure 3.70: One disk of the ETL detector with the layout of the modules and service hybrids (left). A 90-degree section of an ETL disk with cooling inlets and outlets shown at the outer rim (right).

3.7 Mechanical Engineering, Integration, and Installation

A mechanical drawing of the ETL detector is shown in Figure 3.2. The support structures for the detector modules and service hybrids are aluminum disks containing embedded cooling tubes to evacuate the heat generated by the sensors and readout electronics. Each endcap of the ETL detector is comprised of two disks, and both faces of each disk are populated with active elements. This design ensures a high acceptance per disk, such that more than 85% of particles emanating from the interaction region cross the surface of two sensors, providing two independent measurements. Details of the structural design can be found in Section 3.7.1.

ETL modules and service hybrids will be mounted on disks at the Endcap Calorimeter Assembly Facility (ECAF). Once commissioned, the disks will be lowered to the experimental cavern for installation on the front of the CE. The disks will be mounted on the endcap inner support tube shared with the CE, but in an independent cold volume with a thermal screen that can be retracted to allow service and maintenance of the ETL detector. The integration and installation are described in Sections 3.7.2 and Section 3.7.3, respectively.

3.7.1 Structural design

The ETL detector is assembled from disks, as shown in Fig. 3.70 (left). Each disk serves as a mechanical support as well as a cooling plate. The disks are made of $\frac{1}{4}$-inch MIC6 aluminum, in which a small diameter stainless steel tube carries liquid CO_2 to maintain the sensor temperature below $-25\,°C$. A quarter of a cooling disk, referred to as a wedge, is shown in Fig. 3.70 (right). Wedges are machined to permit easy integration of wedges into half-disks, while minimizing the region uncovered by sensors to maximize particle acceptance. Wedges are also machined with holes for the placement of screws or pins used for the mounting of modules and service hybrids.

The inner support tube, shown in Fig. 3.71 (left), is made of a permaglas section supporting the ETL detector, and an aluminum section supporting the electromagnetic sub-detector of the CE. It is located at the inner region of the detector, closest to the beampipe. The tube thermally